Received: 16 September 2022 | Revised: 27 October 2022 | Accepted: 2 November 2022

DOI: 10.1002/smm2.1181

RESEARCH ARTICLE

SmartMat Open Access WILEY

Rapid laser synthesis of surfactantless tantalum-based nanomaterials as bifunctional catalysts for direct peroxide–peroxide fuel cells

Xiaoyong Mo[1] | **Brigitte Bouchet Fabre**[2] | **Nathalie Herlin-Boime**[2] | **Edmund C. M. Tse**[1,3]

[1]HKU-CAS Joint Laboratory on New Materials, Department of Chemistry, University of Hong Kong, Hong Kong SAR, China

[2]NIMBE, CEA, CNRS, CEA Saclay, Université Paris-Saclay, Gif-sur-Yvette, France

[3]HKU Zhejiang Institute of Research and Innovation, Zhejiang, China

Correspondence

Nathalie Herlin-Boime, NIMBE, CEA, CNRS, CEA Saclay, Université Paris-Saclay, 91191 Gif-sur-Yvette, France.
Email: nathalie.herlin@cea.fr

Edmund C. M. Tse, HKU-CAS Joint Laboratory on New Materials, Department of Chemistry, University of Hong Kong, Hong Kong SAR, China.
Email: ecmtse@hku.hk

Funding information

Research Grants Council, University Grants Committee, Grant/Award Numbers: 27301120, E-HKU704/19, JLFS/P-704/18; National Natural Science Foundation of China, Grant/Award Number: 22002132; Agence Nationale de la Recherche, Grant/Award Number: ANR-13-IS09-0003

Abstract

Efficient and durable electrocatalysts are instrumental in enabling next-generation fuel cell technologies. At present, expensive precious metals are used as state-of-the-art catalysts. In this report, cost-effective nanosized tantalum-based alternatives are synthesized for the first time via a green and scalable laser pyrolysis method as bifunctional catalysts for direct peroxide–peroxide fuel cells. This rapid laser pyrolysis strategy allows for the production of nanoparticles at a laboratory scale of grams per hour, compatible with a detailed exploration of the functional properties of as-synthesized nanoparticles. By varying the precursor ratio between ammonia and tantalum ethanolate, five tantalum-based nanomaterials (TaNOC) are prepared with crystalline phases of Ta_2O_5, Ta_4N_5, Ta_3N_5, and TaN in tunable ratios. Electrochemical studies in neutral and alkaline conditions demonstrate that Ta_4N_5 is the active component for both H_2O_2 oxidation and reduction. Kinetic isotope effect studies show that protons are involved at or before the rate-determining step. Long-term stability studies indicate that Ta_3N_5 grants surfactant-free TaNOC-enhanced longevity during electrocatalytic operations. Taken together, bifunctional TaNOC can act as active and robust electrocatalysts for H_2O_2 reduction and oxidation. Laser pyrolysis is envisioned to produce refractory metal nanomaterials with boosted corrosion resistance for energy catalysis.

KEYWORDS

bifunctional catalysis, laser pyrolysis, peroxide fuel cells, tantalum nanomaterials

1 | INTRODUCTION

Next-generation fuel cell technology is one of the key components of a future society powered by clean energy.[1–3] Regarding the selection of renewable fuels for energy conversion, H_2O_2 is considered a sustainable power source in a direct hydrogen peroxide/hydrogen peroxide fuel cell (DPPFC).[4–6] The $2e^-$ $2H^+$ reduction and oxidation products of H_2O_2 are O_2 and H_2O (Equations 1 and 2), which are both environmentally benign and can be used readily in industrial processes. Since H_2O_2 reacts at both the cathode and anode, DPPFC can take advantage of a single-chamber design that significantly simplifies the overall architecture of the fuel cell stack.[7] These advantageous attributes enable DPPFC an up-and-coming technology for mass transportation

$$H_2O_2 + 2H^+ + 2e^- \rightarrow 2\,H_2O \rightarrow E^0 = 1.776\ \text{V versus RHE}, \quad (1)$$

$$H_2O_2 \rightarrow O_2 + 2H^+ + 2e^- \rightarrow E^0 = 0.695\ \text{V versus RHE}. \quad (2)$$

Ample efforts have been invested into fabricating nanomaterials composed of noble metals,[4,8–13] late transition metal oxides,[14,15] and coordination complexes[16,17] to enhance the overall efficiency of fuel cells.[16] Typically, these metal oxides and complexes have been used for H_2O_2 reduction, while they are rarely applied to H_2O_2 oxidation likely due to their limited robustness under harsh operating environments.[18] Though robust noble metals with outstanding catalytic activity can overcome the stability challenge, their prohibitive costs have hindered their widespread applications in the fuel cell industry.[19,20] Alternatively, early transition metals have rarely been applied to facilitate H_2O_2 redox reactions, though Ti and V have found practical uses in polymerization and redox flow batteries.[21,22] Early transition metals, such as Ta, in their oxidized forms can serve as enticing candidates for DPPFCs.

Apart from the choice of nanomaterials, the synthesis methods adopted to produce these catalysts could play an essential role in determining whether DPPFCs will be successfully implemented in future societies.[23] Typically, high temperatures at elevated pressures are required to generate nanocatalysts in batches with the emission of toxic liquid wastes.[24–27] These energy-intensive and environment-damaging strategies hinder the realization of emerging DPPFC technologies.[28] Recently, laser-based techniques, such as pulsed laser ablation and laser direct writing, have been demonstrated to be prominent nanofabrication methodologies.[29–32] Among these techniques, laser pyrolysis stands out as an efficient technology to produce nanomaterials in a green manner without toxic liquid effluents.

Here, a rapid laser pyrolysis method is developed to synthesize tantalum-based nanomaterials (TaNOC) as a new class of bifunctional catalysts for H_2O_2 oxidation and reduction for DPPFCs. The obtained TaNOC nanocomposites containing various amounts of N and O are prepared using a CO_2 laser in a custom-built system operating at atmospheric pressure. These surfactant-free TaNOC nanocomposites with tunable ratios of Ta_2O_5, Ta_4N_5, Ta_3N_5, and TaN phases display prominent catalytic activities toward H_2O_2 oxidation and reduction. This exploratory work serves as a milestone for developing early transition metal materials for sustainable energy catalysis and renewable power schemes in the future.

2 | EXPERIMENTAL SECTION

2.1 | General methods

Reagents were purchased from commercial sources and used without further purification, unless otherwise noted. All aqueous solutions were prepared using Millipore water (18.2 MΩ cm).[29] For synthesis, 60 wt% tantalum ethanolate ($Ta(OCH_2CH_3)_5$, 99.8% purity; Sigma) was dissolved in 40 wt% toluene (99.8% purity; Merck). Gaseous NH_3 (99% purity; Air Liquide) was used during the laser pyrolysis step. Experiments at pH 7 were performed in 100 mmol/L phosphate buffer prepared using NaH_2PO_4 (ACS reagent grade; J&K Scientific) and Na_2HPO_4 (ACS reagent grade; J&K Scientific). Experiments at pH 13 were performed in 100 mmol/L NaOH (analytical grade; Merck Millipore) dissolved in Milli-Q water. Solutions were sparged with N_2 (99.995% high purity grade; Linde HKO) for 30 min before each experiment following published methods.[33] For electrochemical studies, 50 mmol/L H_2O_2 (AnalaR NORMAPUR; VWR) was added to the electrolyte solution.

2.2 | Catalyst preparation

Samples TaNOC-1, TaNOC-2, TaNOC-3, TaNOC-4, and TaNOC-5 were prepared by laser pyrolysis using a published protocol.[34,35] Briefly, toluene droplets containing tantalum ethanolate were generated using a custom pyrosol device. These droplets were carried by a flow of NH_3, Ar, or Ar/NH_3 mixture to the reaction zone where they interacted with a high-power CO_2 laser beam.

Specifically, the reactant droplets entered the reactor through a 10-mm wide tube and intersected with the laser beam about 2 mm above the inlet tube. Moreover, the confinement enabled by the Ar flow around the reactant flow avoided the dispersion of the reactant and ensured that the reactants were well covered by the laser beam (see Supporting Information: Figure S25 for the laser beam geometry). Upon dissociation of the precursors, nanoparticles containing Ta, N, O, and C were formed via nucleation and growth. TaNOC-2 was further annealed at 300 °C under air to yield TaNOC-2P.[34,36]

2.3 | Material characterization

Powder X-ray diffraction (PXRD) was conducted on a Rigaku MiniFlex 600-C X-ray diffractometer with peak identification using the ICDD database. Transmission electron microscopy (TEM) and energy-dispersive X-ray spectroscopy (EDS) were conducted using an FEI Tecnai G2 20 S-TWIN scanning transmission electron microscope. High-angle annular dark-field STEM (HAADF-STEM), and HAADF-STEM-EDS mapping were examined using a Thermo Scientific Talos F200XFEG STEM.[37] Scanning electron microscopy (SEM) was performed on a Hitachi S4800 field emission scanning electron microscope, and the collected images were analyzed following a published method.[29] Surface elemental mapping was conducted on the SEM equipped with an Oxford instruments EDS detector, and the recorded data were analyzed using Aztec software.[38]

X-ray photoelectron spectroscopy (XPS) was performed on a Thermo Scientific ESCALAB XI^+ X-ray photoelectron spectrometer microprobe with a monochromatic Al Kα X-ray source ($h\nu = 1486.6$ eV) and a Kratos Analytical Axis Ultra DLD spectrometer with monochromatic Al Kα X-ray ($h\nu = 1486.6$ eV). Curve-fitting analysis was conducted on Casa XPS software following a published protocol.[39] Carbon content was measured using a Horiba EMIA analyzer without any special treatment on the sample powders.

2.4 | Ink preparation

Finely ground TaNOC-1, TaNOC-2, TaNOC-3, TaNOC-4, TaNOC-5, and TaNOC-2P (4 mg) were suspended and sonicated in 1 mL ethanol (Scharlau; Abs) for 20 min, respectively. Nafion perfluorinated resin solution (4 μL, 5 wt% in lower aliphatic alcohols with 15 − 20% water; Sigma-Aldrich) was added into the ethanolic well-dispersed catalyst mixture. The resulting mixture was continuously sonicated for 10 min to form inks. Ten microliters of the as-prepared ink was drop-casted onto a glassy carbon (GC) disk electrode ($A = 0.196$ cm^2), which was polished using 3–0.5 μm alumina suspension.

2.5 | Electrochemical measurements

All electrochemical experiments were conducted using a CH Instruments 760E bipotentiostat in a three-electrode configuration at room temperature following published procedures.[40] The counter electrode was a graphite rod, while the reference electrode was an Ag/AgCl (3 mol/L KCl) assembly. All potentials were measured against the Ag/AgCl reference electrode and converted to a reversible hydrogen electrode (RHE) based on the Nernst equation.[41]

2.6 | Kinetic isotope effect (KIE) studies

All deutero aqueous solutions were prepared using D_2O (D, 99.9%; Cambridge Isotope Laboratories, Inc.). Experiments at pD 7 (where pD = –log[D^+]) were conducted in deutero Britton–Robinson buffer solution containing boric acid (40 μmol/L, 99.999%; Fisher Scientific), acetic acid (40 μmol/L, 100%; VWR), D_3PO_4 (40 μmol/L, 85 wt% in D_2O; J&K Scientific), and $NaClO_4$ (100 mmol/L, 99.9%; Sigma-Aldrich). For experiments at pD 13, 100 mmol/L NaOD (Energy Chemical) solutions were used.[42]

3 | RESULTS AND DISCUSSION

3.1 | Design and fabrication of TaNOC nanocomposites

3.1.1 | Preparation of TaNOC

To develop a new class of early transition metal materials for fuel cell applications, rapid laser pyrolysis is used to generate TaNOC using Ta(V) ethanolate and toluene precursors in a scalable one-step process (Figure 1). Supporting Information: Table S1 presents the main laser pyrolysis parameters, including laser power, gas flow rate, and ammonia/argon gas ratio, used to fabricate tantalum-based nanomaterials (TaNOC-x) ($x = 1$–5) samples. Supporting Information: Table S1 also shows the production rate and carbon content of pristine TaNOC-x powders. All collected TaNOC-x powders are black in color, an observation that is in agreement with the presence of carbon. Since all production rates of TaNOC-x exceeded 5 g/h, only 40–45 min is needed to produce

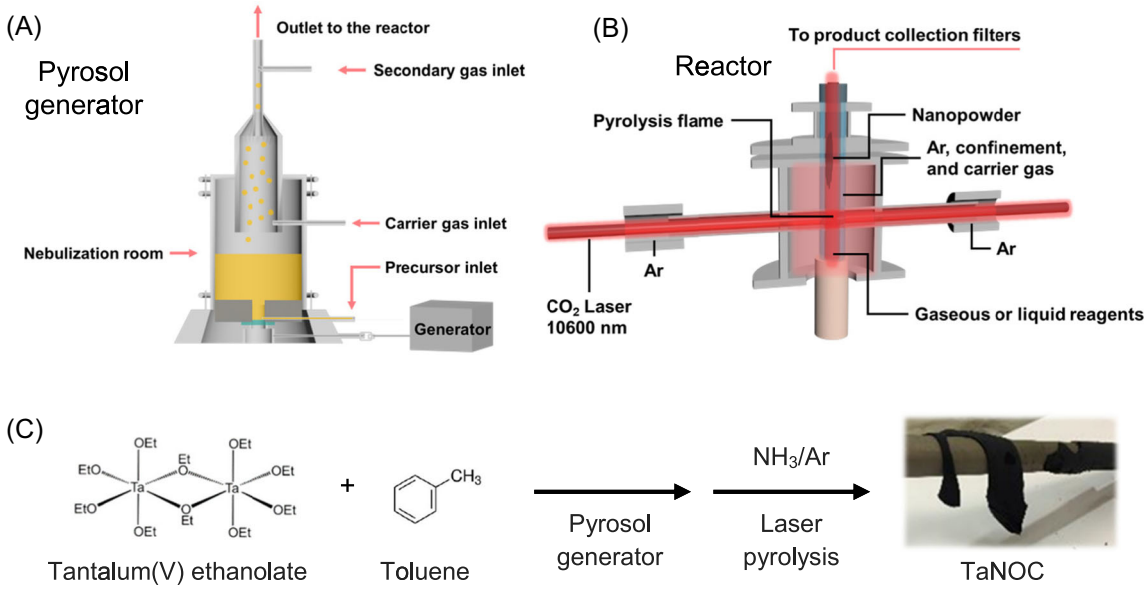

FIGURE 1 (A) Depiction of the pyrosol generator that uses Ta(V) ethanolate and toluene as precursors in a 3:2 mass ratio. (B) Illustration of a custom-built laser pyrolysis reactor for the synthesis of TaNOC nanocomposites using a 10,600 nm CO_2 laser. (C) Overall preparation scheme of TaNOC using Ar and NH_3 as the carrier gas mixture. TaNOC, tantalum-based nanomaterial.

TaNOC-*x* in sufficient quantity for all subsequent experiments, demonstrating the efficiency of this tunable approach.

Comparing TaNOC-1 and TaNOC-2, both the production rate and carbon content increase upon the introduction of 10% NH_3 into the reaction zone. This observation can be rationalized as follows. Upon elevating the NH_3 content in the reaction chamber, the absorbed laser power increases correspondingly, suggesting that the laser radiation is absorbed by gas-phase NH_3 molecules. Due to a boost in laser power absorption, the temperature of the flame in the laser pyrolysis reactor increases as well, thus leading to a more complete dissociation of the tantalum ethanolate and toluene precursors. Subsequently, more pristine powder with a higher C content is produced within a given period of time.

Intriguingly, upon increasing the NH_3 content beyond 10%, the measured production rate decreases while the carbon content also dwindles (from TaNOC-2 to TaNOC-5). To understand this reverse trend up to 40% NH_3 added, the effect of the Ar carrier gas needs to be taken into account. Ar is the most effective inert gas to serve as a medium and a transfer agent for the precursors and NH_3 to react. Upon raising the NH_3:Ar ratio, the relative amount of Ar decreases, thereby decreasing the efficiency of droplets containing carbonaceous species being transferred to the reaction zone. Lesser precursor droplets transferred to the laser cross-section further lead to a reduction in the C:N ratio in the reaction zone, resulting in a decline in the overall production rate as well as a drop in the resulting carbon content observed. Interestingly, this drop is in good correlation with a concurrent increase in the N content (see Supporting Information: Table S2). A postannealing protocol at 300 °C under air is applied to activate TaNOC-2 by partially removing the amorphous carbon. TaNOC-2 with the highest carbon content shows a four-fold decrease in C:Ta ratio upon annealing as quantified by elemental analysis (EA).

3.1.2 | Chemical composition and structural analysis of TaNOC

XRD is used to examine the crystallinity of TaNOC nanomaterials. Figure 2A and Supporting Information: Figure S1 show the XRD diffraction patterns of TaNOC-*x* indexed according to the crystalline phases recorded in the ICDD database (Ta_2O_5 #19-1299, Ta_4N_5 #50-1176, Ta_3N_5 #79-1533, and TaN #49-1283). XRD data show that TaNOC-1 exhibits a diffraction pattern similar to that of a pure Ta_2O_5 phase. With an increase in the NH_3 used during laser pyrolysis, the intensity of the Ta_2O_5 diffraction pattern diminishes. As the N content in the TaNOC-*x* powder increases, the signals for nitrided phases such as Ta_4N_5, Ta_3N_5, and TaN grow substantially. When the NH_3:Ar ratio reaches 40:60, Ta_2O_5 disappears completely while metallic TaN becomes the major component (Supporting Information: Table S3). These XRD results demonstrate that the components within TaNOC-*x* samples can be tuned through the use of this modular laser pyrolysis technique.

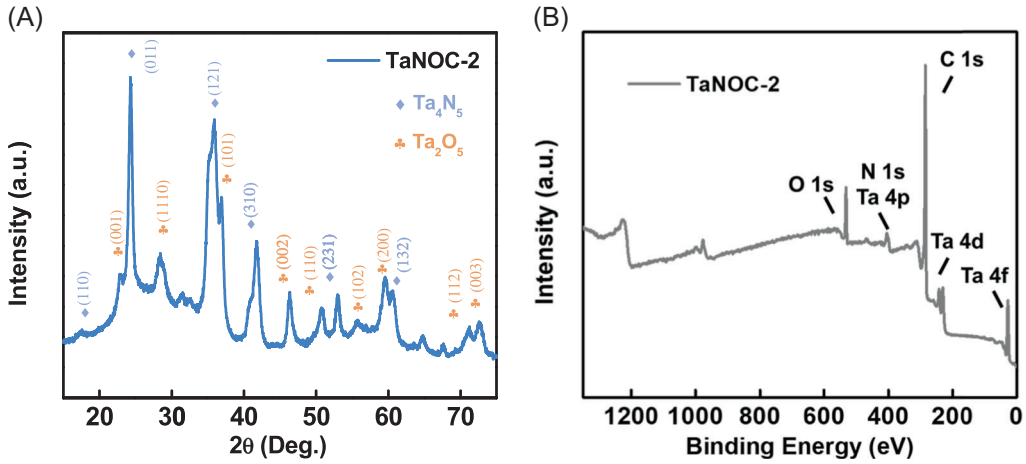

FIGURE 2 (A) X-ray diffraction pattern and (B) X-ray photoelectron spectroscopy survey scan of TaNOC-2. TaNOC, tantalum-based nanomaterial.

The chemical compositions and valence states of TaNOC-*x* are analyzed using XPS.[43] High-resolution XPS of Ta 4f in TaNOC-2 and TaNOC-3 display similar species that contain Ta–O and Ta–N (Supporting Information: Figures S2A and S3A). These two species are also verified in Ta 4p, which are shown in Supporting Information: Figures S2B and S3B. Despite the morphologies and chemical compositions of TaNOC-2 and TaNOC-3 illustrating the same pattern, the XPS signal of Ta–O and Ta–N species show differences with a more intensive Ta–N peak in TaNOC-3. This result indicates that TaNOC-3 contains more tantalum nitride species than TaNOC-2. Supporting Information: Table S3 summarizes the evolution of C, N, and Ta content of the TaNOC-*x* samples obtained from XPS measurements. Two experimental trends are observed. First, the C content decreases with the C/Ta ratio. Second, as the NH_3 flow increases, the N/Ta ratio increases correspondingly. Taking these XPS data together, the chemical composition of TaNOC-*x* samples can be regulated by controlling the gas-phase reaction condition within the laser chambers.

The nanostructures of the pristine TaNOC-*x* powders are examined using TEM. Figure 3 and Supporting Information: Figure S4 show that TaNOC-*x* samples contain core-shell nanospheres with particle sizes ranging from 7.91 to 23.56 nm. The particle size increases with the amount of Ta_2O_5 present in the TaNOC-*x* samples. Figure 3C,D illustrates that TaNOC-2 contains a carbon shell with a core comprising of well-distributed Ta, N, and O, indicating that tantalum oxide and tantalum nitride are formed and wrapped by carbon. SEM images shown in Figure 4 and Supporting Information: Figures S5–S8 further demonstrate that there is no significant difference in the morphology of the TaNOC-*x* powders. Energy-dispersive X-ray spectroscopy (EDX) elemental mapping shows that Ta, N, O, and C are evenly distributed in TaNOC-*x* samples. The unique hierarchical structures of TaNOC-*x* could be beneficial toward electrocatalysis.

3.2 | Electrocatalytic activities of TaNOC nanocomposites

3.2.1 | Electrochemical H_2O_2 reduction

Next, the electrocatalytic performance of the as-prepared TaNOC is examined. Figure 5A shows the linear sweep voltammograms (LSVs) of GC electrodes modified with TaNOC-1, TaNOC-2, TaNOC-3, TaNOC-4, and TaNOC-5 at pH 7. TaNOC-2 displays the most positive onset potential for H_2O_2 reduction at 0.37 V versus RHE among the Ta-based materials synthesized (Figure 5A, blue line), followed by TaNOC-3, then TaNOC-4, and lastly TaNOC-5 and TaNOC-1. In addition to showing an early-onset potential, TaNOC-2 also displays a sizeable H_2O_2 reduction current density of 0.53 mA/cm^2 measured at 0 V versus RHE (Figure 5B), highest among the samples tested, followed by TaNOC-3, then TaNOC-5, TaNOC-4, and lastly TaNOC-1. In short, TaNOC-2 is an efficient H_2O_2 reduction electrocatalyst that features an early transition metal at neutral pH.

Analogous H_2O_2 reduction performance trends are observed in an alkaline environment (Figure 6B). TaNOC-2 exhibits an onset potential at 0.43 V versus RHE (Figure 6A, blue line), with the highest reduction current density at pH 13. In both neutral and basic conditions, TaNOC-1 and TaNOC-5 display poor H_2O_2 reduction activities, suggesting that Ta_2O_5, Ta_3N_5, and TaN are not catalytically active. TaNOC-2 exhibits an outstanding H_2O_2 reduction performance at both

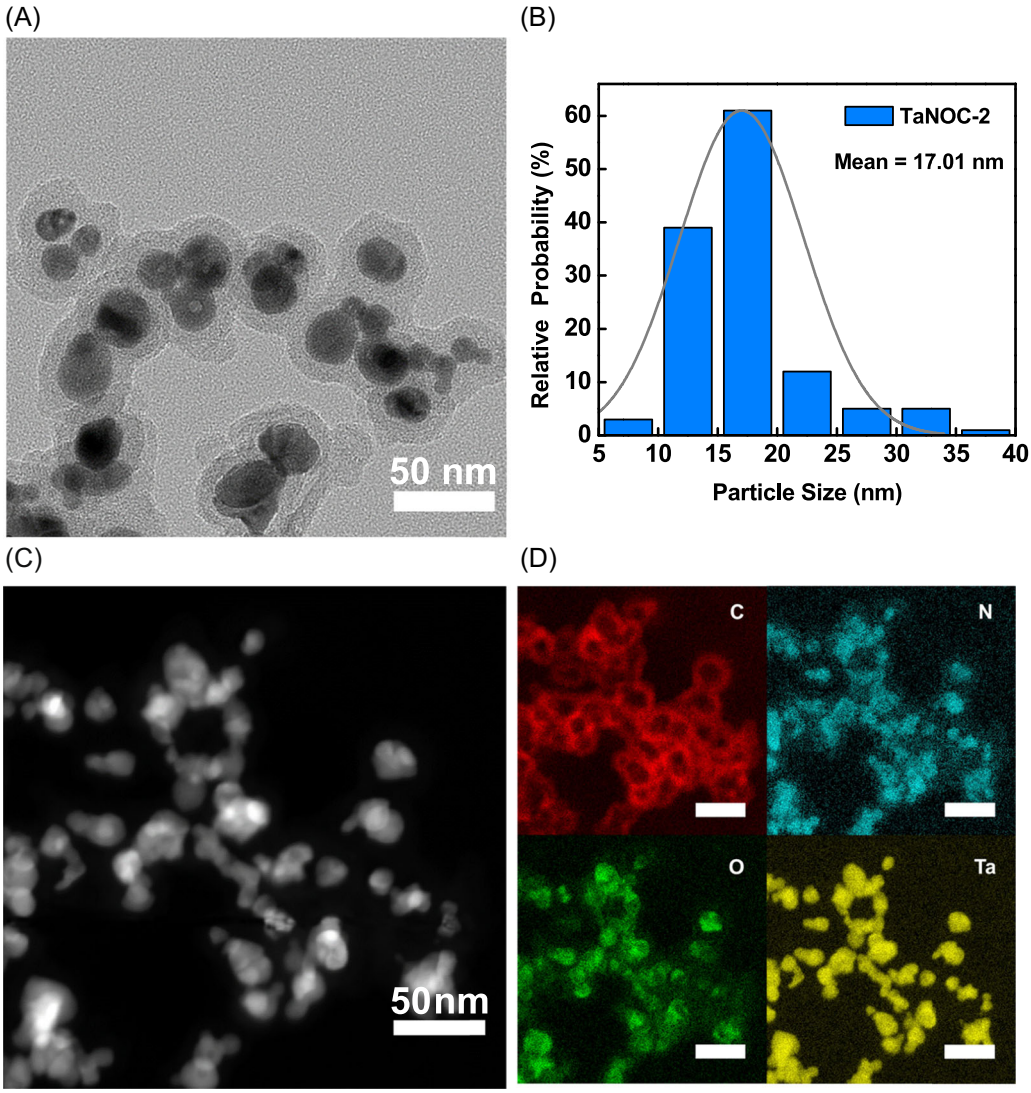

FIGURE 3 (A) Transmission electron microscopy, (B) particle size distribution, (C) high-angle annular dark-field STEM image, and (D) STEM-energy-dispersive X-ray spectroscopy elemental mapping of C, N, O, and Ta in TaNOC-2. STEM, scanning transmission electron microscope; TaNOC, tantalum-based nanomaterial.

pH 7 and 13, indicating that Ta_4N_5 acts as the primary catalytically active site in TaNOC nanomaterials prepared using laser pyrolysis.

3.2.2 | Electrochemical H_2O_2 oxidation

To investigate whether TaNOC nanocomposites are capable of acting as bifunctional catalysts in DPPFCs, the H_2O_2 oxidation activities of as-prepared TaNOC-*x* nanocomposites are next explored. At pH 7, among the as-prepared Ta materials, TaNOC-2 and TaNOC-3 display similar onset potentials at 1.2 V versus RHE, while TaNOC-1, TaNOC-4, and TaNOC-5 exhibit similar late-onset potentials. Figure 7B summarizes the H_2O_2 oxidation activities of all the Ta-based electrocatalysts studied here. TaNOC-3 and TaNOC-2 display the highest current densities measured at 1.3 V versus RHE (0.25 and 0.21 mA/cm^2). In short, in addition to being prominent H_2O_2 reduction catalysts, TaNOC-2P and TaNOC-3P can also oxidize H_2O_2 efficiently in neutral conditions.

The H_2O_2 oxidation performance of our electrocatalysts at pH 13 is next explored. Figure 8A shows the LSVs of TaNOC nanocomposites in the presence of H_2O_2 under basic conditions. TaNOC-2 and TaNOC-3 display the most promising onset potential at 1.0 V versus RHE among all samples. Figure 8B summarizes the H_2O_2 oxidation activities of the series of TaNOC-*x* samples in an alkaline environment. TaNOC-2 displays the highest current densities among all samples tested (0.82 mA/cm^2 measured at 1.3 V vs. RHE). Taking together the electrocatalytic performance results, TaNOC-2 displays the most favorable onset potentials and reaction kinetics for both the oxidation and reduction of

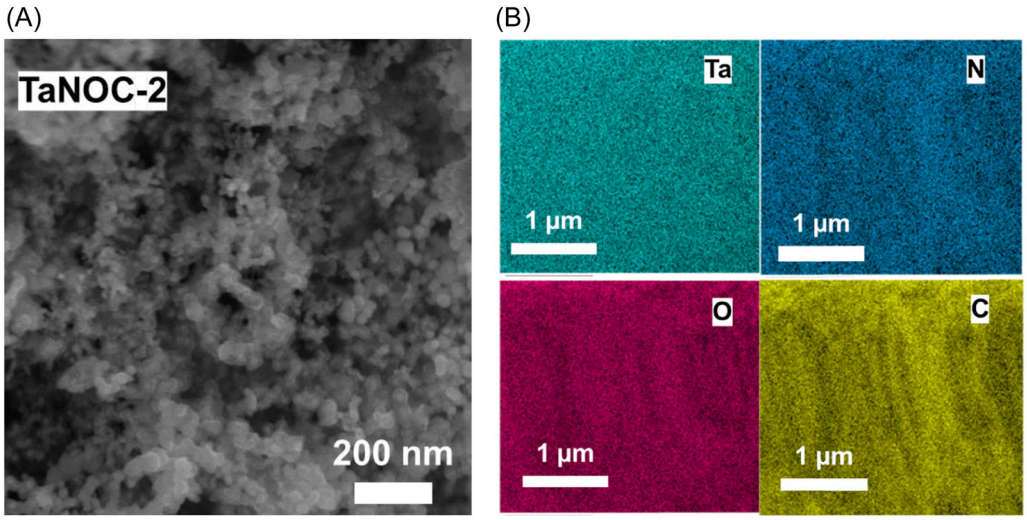

FIGURE 4 (A) Scanning electron microscopy image and (B) elemental mapping with the areal distribution of Ta, N, O, and C of TaNOC-2. TaNOC, tantalum-based nanomaterial.

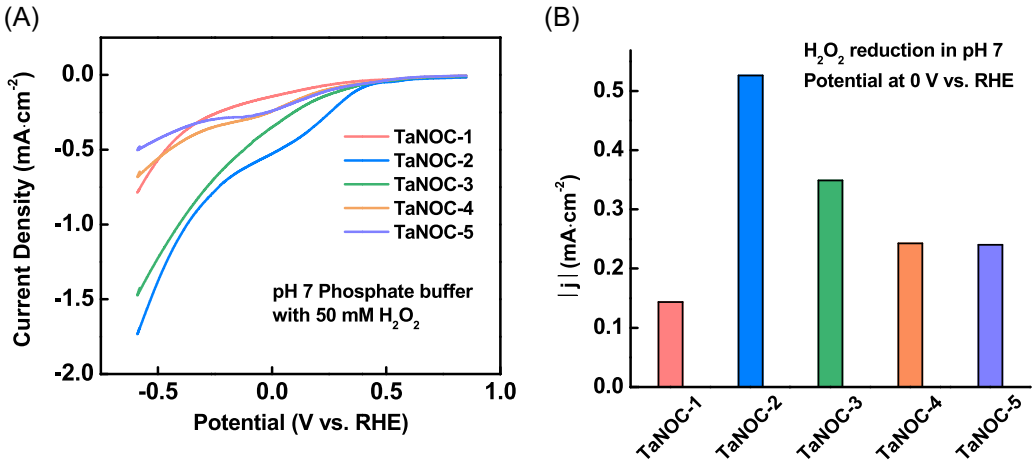

FIGURE 5 (A) H_2O_2 reduction linear sweep voltammograms of TaNOC-1 (red), TaNOC-2 (blue), TaNOC-3 (green), TaNOC-4 (orange), TaNOC-5 (purple) in (A) N_2-saturated pH 7 phosphate buffer with 50 mmol/L H_2O_2. (B) H_2O_2 reduction activity of our catalysts in pH 7 buffer at 0 V versus RHE. RHE, reversible hydrogen electrode; TaNOC, tantalum-based nanomaterial.

H_2O_2 in neutral and basic conditions. TaNOC-1 and TaNOC-5 exhibit low H_2O_2 oxidation activities at pH 7 and 13, suggesting that Ta_2O_5, Ta_3N_5, and TaN are catalytically inactive. Under neutral and alkaline environments, TaNOC-2 displays superb H_2O_2 oxidation performance, indicating that Ta_4N_5 is a major catalytic component in laser-fabricated Ta/N/O nanomaterials.

3.2.3 | Enhancing the H_2O_2 reduction and oxidation performance of TaNOC-2 through postannealing

Since TaNOC-2 exhibits excellent performance in the catalytic reduction and oxidation of H_2O_2 in both pH 7 and pH 13, TaNOC-2 is subjected to a postheat treatment process to generate TaNOC-2P in hopes of further boosting its electrocatalytic activity. The structural and compositional changes in TaNOC-2P after receiving thermal treatment are investigated using a suite of physical and chemical characterization techniques (Figure 9 and Supporting Information: Figure S9). Figure 9A and Supporting Information: Figure S9A show the microstructures of TaNOC-2P. The SEM image of TaNOC-2P is similar to that of TaNOC-2, suggesting that there is minimal difference in the overall morphology of the nanocomposites before and after heat treatment (Supporting Information: Figure S9A). The TEM image of TaNOC-2P reveals that the core-shell structure of TaNOC-2 is still maintained after annealing at 300 °C in

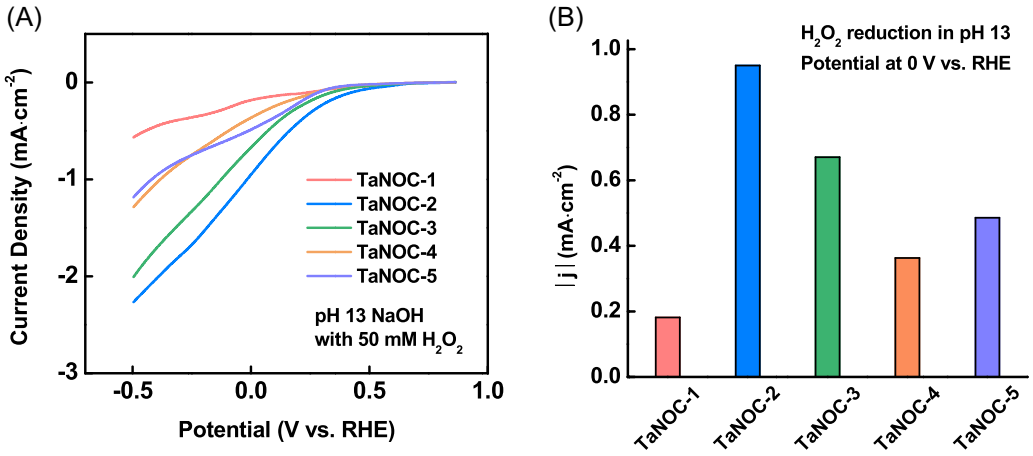

FIGURE 6 (A) H_2O_2 reduction linear sweep voltammograms of TaNOC-1 (red), TaNOC-2 (blue), TaNOC-3 (green), TaNOC-4 (orange), TaNOC-5 (purple) in N_2-saturated pH 13 NaOH with 50 mmol/L H_2O_2. (B) H_2O_2 reduction activity of our catalysts in pH 13 solution at 0 V versus RHE. RHE, reversible hydrogen electrode; TaNOC, tantalum-based nanomaterial.

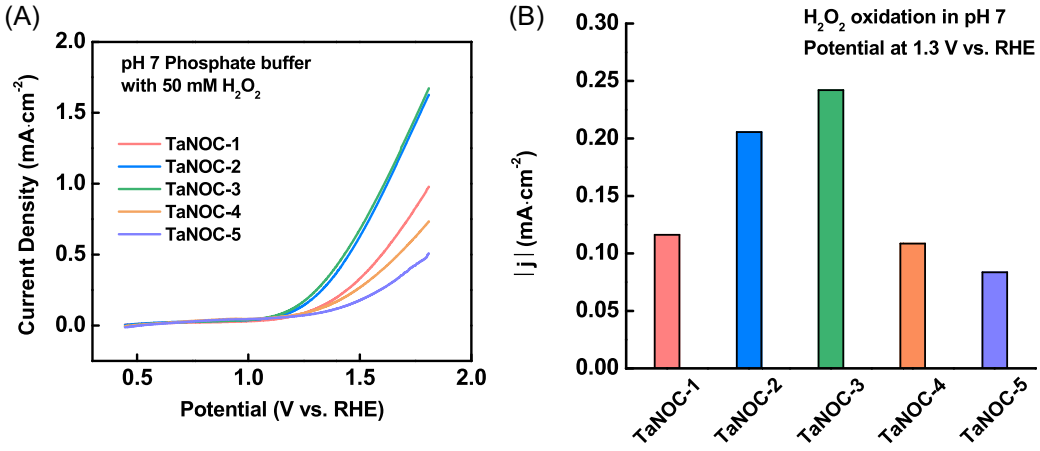

FIGURE 7 (A) H_2O_2 oxidation linear sweep voltammograms of TaNOC-1 (red), TaNOC-2 (blue), TaNOC-3 (green), TaNOC-4 (orange), TaNOC-5 (purple) in N_2-saturated pH 7 phosphate buffer with 50 mmol/L H_2O_2. (B) H_2O_2 oxidation activity of our catalysts in pH 7 buffer at 1.3 V versus RHE. RHE, reversible hydrogen electrode; TaNOC, tantalum-based nanomaterial.

air. The particle size of TaNOC-2P decreases slightly to an average diameter of 16 nm (Figure 9B), which is 2 nm smaller than its untreated version. The shrunk particle size results in an increase in the surface area, a feature that is conducive to higher electrocatalytic performance for H_2O_2 reduction and oxidation.

The change in chemical compositions of TaNOC-2 upon postheat treatment is next examined through HAADF-STEM with EDX (HAADF-STEM-EDX), XPS, and EA. Figure 9C,D shows the HAADF-STEM image and EDX mapping results of TaNOC-2P. The areal mapping results indicate that Ta, N, O, and C are evenly distributed in TaNOC-2P in a manner similar to that in TaNOC-2. HAADF-STEM-EDX mapping shown in Figure 9D verifies that the carbon shell still coats on top of the Ta/N/O core. Supporting Information: Figure S10 shows the overlap mapping images of TaNOC-2 and TaNOC-2P. After postthermal treatment, the carbon signal shows less intensive, likely suggesting that the function of heat treatment is to remove some of the amorphous carbon from the shell.

XPS elemental composition analysis shows few differences between TaNOC-2P and TaNOC-2 in the high-resolution scans of C 1s and O 1s. In the high-resolution Ta 4f and Ta 4p scans, the peak signals for Ta–O and Ta–N become weaker in TaNOC-2P relative to TaNOC-2 (Supporting Information: Figures S11A,B and S2A,B). EA results further show that the carbon content decreases by 21% after postheat treatment, confirming that the main effect of annealing is amorphous carbon removal. The removal of adventitious carbon could increase access to active surfaces for electrocatalysis.

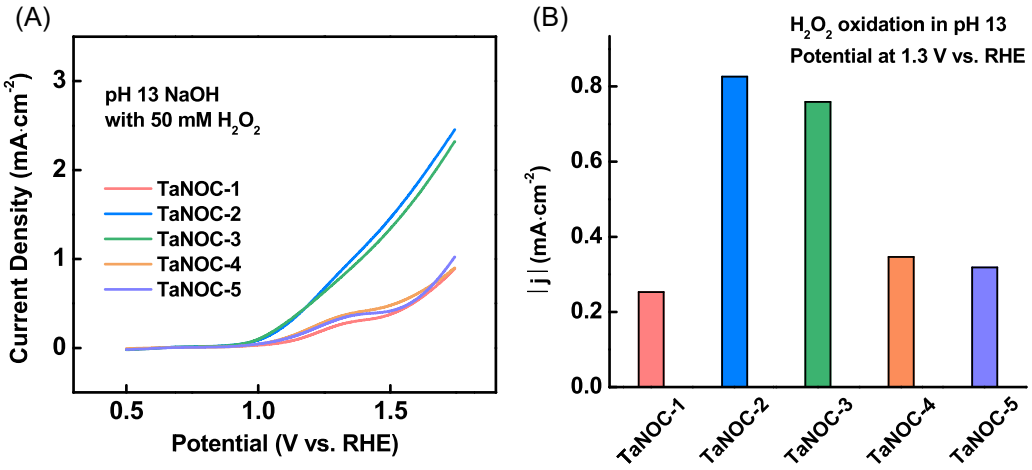

FIGURE 8 (A) H_2O_2 oxidation linear sweep voltammograms of TaNOC-1 (red), TaNOC-2 (blue), TaNOC-3 (green), TaNOC-4 (orange), TaNOC-5 (purple) in N_2-saturated pH 13 NaOH with 50 mmol/L H_2O_2. (B) H_2O_2 oxidation activity of our catalysts in pH 13 solution at 1.3 V versus RHE. RHE, reversible hydrogen electrode; TaNOC, tantalum-based nanomaterial.

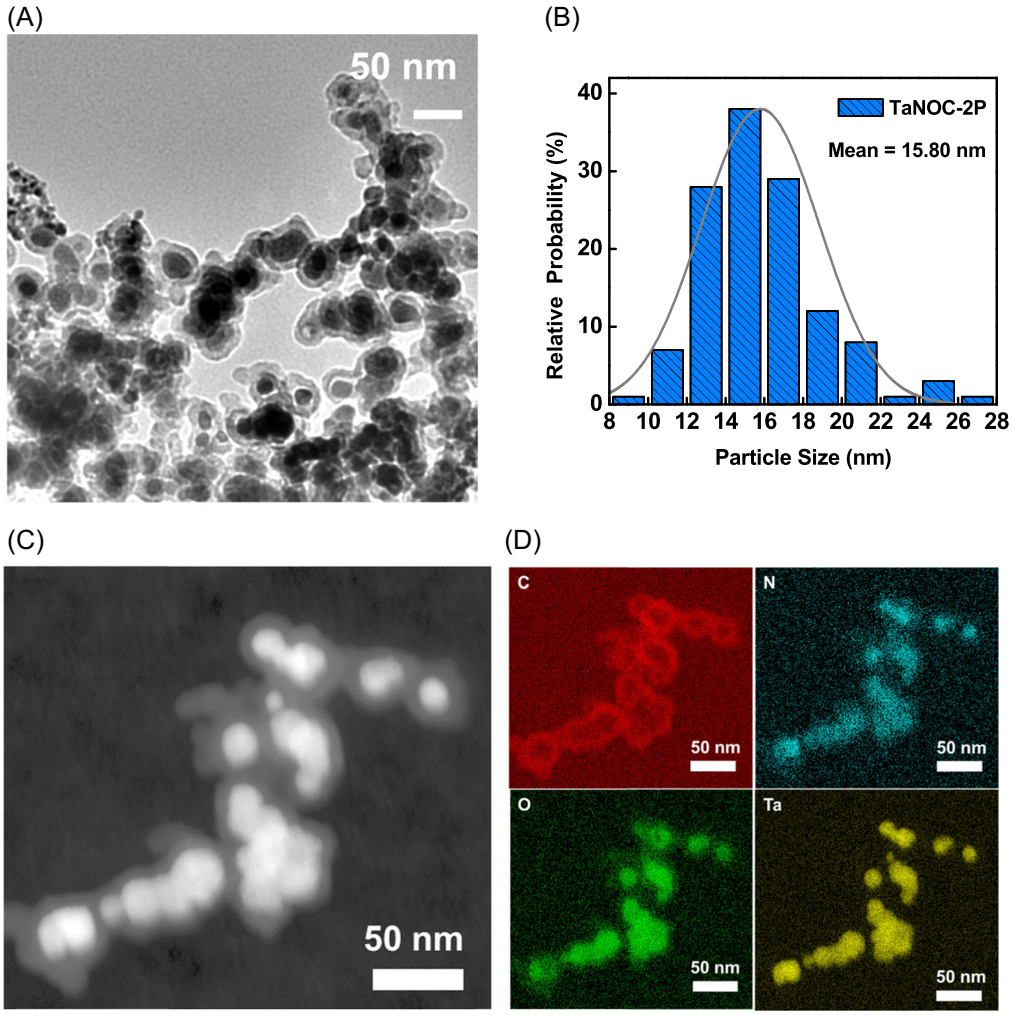

FIGURE 9 (A) Transmission electron microscopy, (B) particle size distribution of TaNOC-2P, (C) HAADF-STEM image of TaNOC-2P, and (D) HAADF-STEM-energy-dispersive X-ray spectroscopy mapping of C, N, O, and Ta in TaNOC-2P. HAADF-STEM, high-angle annular dark-field scanning transmission electron microscope; TaNOC, tantalum-based nanomaterial.

XRD is next utilized to further interrogate changes to the phases present in the heat-treated Ta-based nanocomposite. TaNOC-2P displays more diffraction peaks than TaNOC-2 (Supporting Information: Figure S12), suggesting that new crystalline phases have developed. These new phases include two kinds of Ta_2O_5 (#33-1390 and #25-0922) and a new type of Ta_2O_5 (hexagonal), which could lead to enhanced electrocatalytic activity. In addition to the presence of new oxide phases, the amount of Ta–N species in TaNOC-2P has decreased relative to TaNOC-2. Taken together, the postheat treatment process results in smaller nanoparticles with lower carbon content and lesser Ta-N phases as well as gives rise to new oxide phases. These changes in morphology, size, elemental composition, and crystallinity upon annealing might be beneficial for improving the electrocatalytic performance of TaNOC-2P toward H_2O_2 reduction and oxidation.

The relationships between redox activity and changes in physicochemical properties such as microstructure and composition are next investigated. Figure 10 shows the H_2O_2 reduction electrochemical results. The thermally treated TaNOC-2P shows a more positive onset potential (Figure 10A,C) relative to TaNOC-2 as well as triple and twice the current density of TaNOC-2 at 0 V versus RHE in pH 7 and pH 13, respectively (Figure 10B,D). The H_2O_2 reduction onset potential of TaNOC-2P at 0.51 V versus RHE at pH 7 is comparable with state-of-the-art Fe/Co/Ag-based catalysts (Supporting Information: Table S4). Additionally, the onset potential displayed by TaNOC-2P at 0.62 V versus RHE at pH 13 can compete with that by CuO/Pt-based catalyst (Supporting Information: Table S4).

The H_2O_2 oxidation performance of TaNOC-2P is next explored (Figure 11). TaNOC-2P exhibits a promising onset potential for H_2O_2 oxidation at 1.1 V versus RHE in neutral conditions (Figure 11A), a value that is comparable to state-of-the-art MnO_2/Co_3O_4-based catalysts (Supporting Information: Table S5). TaNOC-2P also exhibits high current density (0.55 mA/cm^2 obtained at 1.3 V vs. RHE) than TaNOC-2 (Figure 11B). Analogously, TaNOC-2P displays a more onset potential and a higher current density when compared with its nonannealed version (2.4 mA/cm^2 measured at 1.3 V vs. RHE) in pH

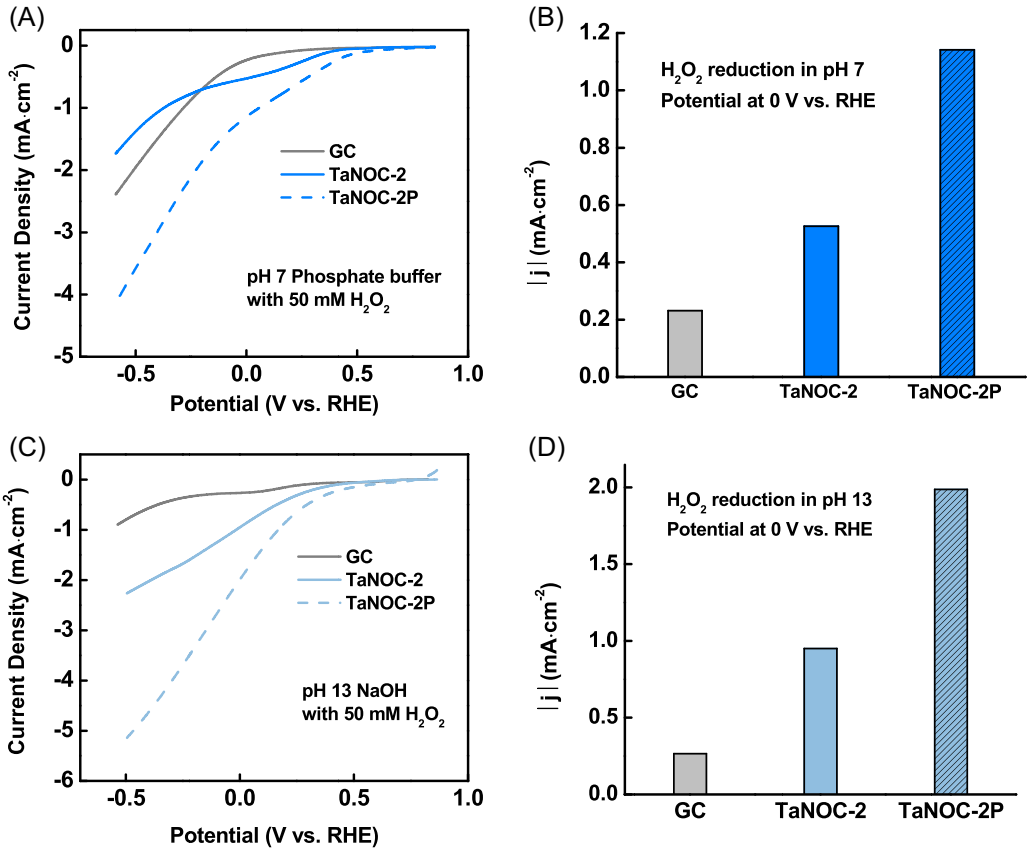

FIGURE 10 (A) H_2O_2 reduction linear sweep voltammogram curves of glassy carbon (GC) (gray), TaNOC-2 (blue, solid) and TaNOC-2P (blue, dash) in pH 7, (B) H_2O_2 reduction activity of TaNOC-2 and TaNOC-2P in pH 7 solution at 0 V versus RHE, (C) H_2O_2 reduction LSV curves of GC (gray), TaNOC-2 (light blue, solid) and TaNOC-2P (light blue, dash) in pH 13, and (D) H_2O_2 reduction activity of TaNOC-2 and TaNOC-2P in pH 13 solution at 1.3 V versus RHE. RHE, reversible hydrogen electrode; TaNOC, tantalum-based nanomaterial.

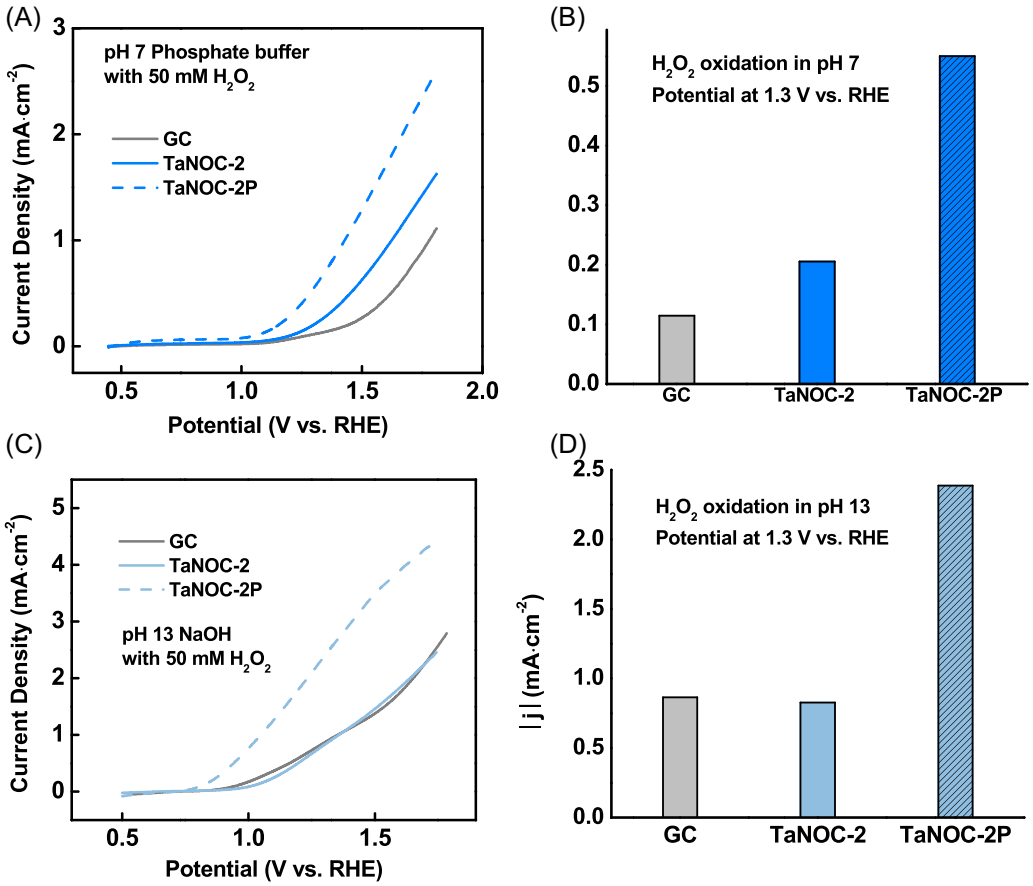

FIGURE 11 (A) H_2O_2 oxidation linear sweep voltammogram curves of GC (gray), TaNOC-2 (blue, solid) and TaNOC-2P (blue, dash) in pH 7, (B) H_2O_2 oxidation activity of GC (gray), TaNOC-2 (light blue, solid) and TaNOC-2P (light blue, dash) in pH 7 solution at 0 V versus reversible hydrogen electrode (RHE), (C) H_2O_2 reduction LSV curves of TaNOC-2 and TaNOC-2P in pH 13, and (D) H_2O_2 reduction activity of TaNOC-2 and TaNOC-2P in pH 13 solution at 1.3 V versus RHE. GC, glassy carbon; RHE, reversible hydrogen electrode; TaNOC, tantalum-based nanomaterial.

13 (Figure 11C,D). Taking together all the electrocatalytic performance results, TaNOC-2P displays the most favorable onset potential and reaction kinetics for both the oxidation and reduction of H_2O_2 in neutral and basic conditions, likely due to the increase in electrocatalytic surface area imbued by nanoparticles of smaller sizes as well as a decrease in amorphous carbon content that renders a more porous shell, faster reactant replenishment, and more efficient product removal.

3.2.4 | Investigating the catalytic pathway on TaNOC-2P

As H_2O_2 reduction contains proton-coupled electron transfer steps, the KIE study is conducted to elucidate the role of protons in the catalytic mechanism. Since TaNOC-2P exhibits the most promising catalytic performance among all the Ta-based materials in this study, LSVs of TaNOC-2P in deuterated solutions are recorded (Supporting Information: Figure S13). TaNOC-2P displays greater H_2O_2 reduction activity in pH 7 buffer relative to that in pD 7 buffer, while the H_2O_2 reduction current density of TaNOC-2P in pH 13 solution is almost five times higher than that in pD 13 solution. Hence, a primary KIE is observed for H_2O_2 reduction catalyzed by TaNOC-2P.

The mechanism by which TaNOC nanomaterials catalyze the oxidation of H_2O_2 is further investigated using KIE. Supporting Information: Figure S14 shows H_2O_2 oxidation LSVs of TaNOC-2P in solutions prepared using normal and heavy water. TaNOC-2P displays current densities at pD 7 around half of those in pH 7. A five-fold decrease in catalytic oxidative currents is observed for TaNOC-2P when pH 13 solution is switched to pD 13 solution. These trends corroborate that a primary KIE is observed for H_2O_2 oxidation catalyzed by TaNOC-2P. Taking together the results from KIE studies, protons are likely involved at or before the rate-determining step of H_2O_2 reduction and oxidation catalyzed by TaNOC-2P.

3.2.5 | Long-term stability study of TaNOC-2P

The long-term stability of laser-synthesized TaNOC nanocomposites is next investigated. Supporting Information: Figure S15A shows the chronopotentiometry (CP) trace of TaNOC-2P at pH 7 holding at a current density of $-2.5\ mA/cm^2$. TaNOC-2P maintains a constant H_2O_2 reduction potential for 23 h. In addition to subjecting TaNOC-2P to CP testing, the post-CP LSV of the TaNOC-2P is also collected (Supporting Information: Figure S15B). Intriguingly, TaNOC-2P displays enhanced H_2O_2 reduction activity after the long-term stability test, likely suggesting that TaNOC-2P can be electrochemically activated.

Supporting Information: Figure S16 shows the long-term stability results of TaNOC-2P at pH 13. TaNOC-2P exhibits stable H_2O_2 reduction potential at an applied current density of $-2.5\ mA/cm^2$ for 23 h. Interestingly, TaNOC-2P displays improved H_2O_2 reduction activities in pH 13 as seen in pH 7. These results demonstrate that TaNOC-2P can be activated by subjecting the samples to a cathodic treatment in both pH 7 and pH 13 conditions.

The durability of TaNOC-2P under H_2O_2 oxidation conditions is next interrogated. Supporting Information: Figure S17A shows the CP traces of TaNOC-2P when held at an anodic current of $2.5\ mA/cm^2$. TaNOC-2P displays stable potential for 23 h. Supporting Information:Figure S17B shows the LSVs of TaNOC-2P before and after subjecting them to a prolonged anodic current holding procedure. Analogous to the two cases above, TaNOC-2P exhibits slightly enhanced H_2O_2 oxidation activities after anodic treatments in pH 7 buffer.

Supporting Information: Figure S18 shows the long-term stability results of TaNOC-2P at pH 13. Under a constant applied current density of $2.5\ mA/cm^2$, TaNOC-2P displays a stable oxidative potential for 23 h (Supporting Information: Figure S18A). Supporting Information: Figure S18B depicts the LSVs of TaNOC-2P before and after their respective long-term stability tests. Analogous to previously tested conditions, TaNOC-2P exhibits enhanced H_2O_2 oxidation activity after anodic treatment. These results together demonstrate that TaNOC-2P is a robust H_2O_2 reduction and oxidation catalyst, and in most cases, its electrocatalytic activities can be enhanced further through either a cathodic or an anodic treatment. TEM images further show that the microstructures of TaNOC-2P remained intact after the stability test (Supporting Information: Figures S19–S22).

TaNOC-2P is next tested for its ability to catalyze the reduction and oxidization of H_2O_2 simultaneously in both pH 7 and pH 13. The results with TaNOC-2P applied on both the cathode and the anode show that TaNOC-2P can perform concomitant H_2O_2 electrocatalysis. Subsequent stability test further demonstrates that this bifunctional TaNOC-2P catalyst can serve as both the cathodic and anodic catalysts to facilitate H_2O_2 reduction and oxidation simultaneously up to 8 h (Supporting Information: Figures S23 and S24). Taken together, the results corroborate that TaNOC-2P is an effective, versatile, and robust electrocatalyst that can enable redox reactions central to realizing a sustainable society powered by renewable energy.

4 | CONCLUSIONS

In this study, a series of TaNOC-*x* with adjustable chemical components were synthesized using a modular laser-pyrolysis method with tunable parameters such as laser power, flow rate, and precursor–carrier gas ratio. Physical and chemical characterization techniques such as XPS, XRD, SEM, TEM, and EDX were conducted to probe the nanostructure, morphology, composition, and valence state of the TaNOC-*x* nanocomposites. These TaNOC nanocomposites were found to be efficient H_2O_2 reduction and oxidation electrocatalysts. Heat-treated Ta/N/O samples display enhanced electrocatalytic performance relative to the nonpyrolyzed materials in both neutral and basic environments. This enhancement is likely due to two major factors: (1) the removal of adventitious surface carbon, thereby exposing more active sites for substrate binding and catalytic turnover, and (2) the decrease in nanoparticle size, thereby increasing electrocatalytic surface area for redox reactions. TaNOC-2P exhibits the most favorable onset potentials and highest current densities, indicating that Ta_4N_5 is the active material for H_2O_2 reduction and oxidation. The activities of TaNOC-2P can be boosted further through the incorporation of a cathodic or anodic treatment. This study demonstrates that TaNOC nanocomposites can serve as nonprecious metal alternatives for advanced direct peroxide-peroxide fuel cells. These highly corrosion-resistant refractory nanomaterials are envisioned to serve as active and robust electrocatalysts in other renewable energy conversion devices.

ACKNOWLEDGMENTS

Edmund C. M. Tse would like to express gratitude to the National Natural Science Foundation of China (NSFC) for providing a Young Scientists Fund (NSFC: 22002132) and the European Union (EU) for sponsoring the SABYDOMA project via the Horizon 2020 program (H2020: 862296) on energy catalysis and sustainable

nanomaterials. Xiaoyong Mo thanks Frankie Y. F. Chan at the Electron Microscope Unit (EMU) at the University of Hong Kong (HKU) for his help with the characterization of nanomaterials. Xiaoyong Mo was supported by an Algaia-HKU Chemistry RPg Award and an SZSTI Basic Science General Program (JCYJ20210324122011031). The authors thank the Research Grants Council (RGC) in Hong Kong (China) for an EU–HK Research and Innovation Cooperation Co-funding Mechanism (RGC: E-HKU704/19), a CAS-RGC Joint Laboratory Funding Scheme (RGC: JLFS/P-704/18), and an Early Career Scheme (RGC: 27301120) for expanding the electrochemical investigation capability as well as upgrading the nanomaterials characterization instruments at the HKU-CAS Joint Laboratory on New Materials. The authors also thank the support provided by the National Research Agency (ANR) through the SNON (Sun light oxi-nitrides for energetic applications project) project reference ANR-13-IS09-0003). The help of two Master students, Laura Line Risal and Shunxing Deng, is gratefully acknowledged. The authors are also grateful to Jocelyne Leroy and Eddy Foy for performing XPS and XRD analyses.

CONFLICTS OF INTEREST

The authors declare no conflicts of interest.

DATA AVAILABILITY STATEMENT

The data that support the findings of this study are available from the corresponding author upon reasonable request.

ORCID

Xiaoyong Mo http://orcid.org/0000-0002-8586-4056
Brigitte Bouchet Fabre http://orcid.org/0000-0003-2728-232X
Nathalie Herlin-Boime http://orcid.org/0000-0003-2214-8551
Edmund C. M. Tse http://orcid.org/0000-0002-9313-1290

REFERENCES

1. Chen C, Sun M, Wang K, Li Y. Dual-metal single-atomic catalyst: the challenge in synthesis, characterization, and mechanistic investigation for electrocatalysis. *SmartMat*. 2022;3(4):533-564.
2. Da Y, Jiang R, Tian Z, Han X, Chen W, Hu W. The applications of single-atom alloys in electrocatalysis: progress and challenges. *SmartMat*. 2023;4(1):e1136.
3. Zhou T, Du Y, Yin S, et al. Nitrogen-doped cobalt phosphate@nanocarbon hybrids for efficient electrocatalytic oxygen reduction. *Energy Environ Sci*. 2016;9(8):2563-2570.
4. Yang F, Cheng K, Mo Y, et al. Direct peroxide–peroxide fuel cell—part 1: the anode and cathode catalyst of carbon fiber cloth supported dendritic Pd. *J Power Sources*. 2012;217:562-568.
5. Mousavi Shaegh SA, Nguyen N-T, Mousavi Ehteshami SM, Chan SH. A membraneless hydrogen peroxide fuel cell using Prussian Blue as cathode material. *Energy Environ Sci*. 2012;5(8):8225-8228.
6. Yamada Y, Yoshida S, Honda T, Fukuzumi S. Protonated iron–phthalocyanine complex used for cathode material of a hydrogen peroxide fuel cell operated under acidic conditions. *Energy Environ Sci*. 2011;4(8):2822-2825.
7. Yang F, Cheng K, Xue X, Yin J, Wang G, Cao D. Three-dimensional porous Ni film electrodeposited on Ni foam: high performance and low-cost catalytic electrode for H_2O_2 electrooxidation in KOH solution. *Electrochim Acta*. 2013;107:194-199.
8. Cao D, Gao Y, Wang G, Miao R, Liu Y. A direct $NaBH_4$–H_2O_2 fuel cell using Ni foam supported Au nanoparticles as electrodes. *Int J Hydrogen Energy*. 2010;35(2):807-813.
9. Tse ECM, Gewirth AA. Effect of temperature and pressure on the kinetics of the oxygen reduction reaction. *J Phys Chem A*. 2015;119(8):1246-1255.
10. Liu G, Young KL, Liao X, Personick ML, Mirkin CA. Anisotropic nanoparticles as shape-directing catalysts for the chemical etching of silicon. *J Am Chem Soc*. 2013;135(33):12196-12199.
11. Chen P-C, Liu G, Zhou Y, et al. Tip-directed synthesis of multimetallic nanoparticles. *J Am Chem Soc*. 2015;137(28):9167-9173.
12. Zhang J, Vukmirovic MB, Xu Y, Mavrikakis M, Adzic RR. Controlling the catalytic activity of platinum-monolayer electrocatalysts for oxygen reduction with different substrates. *Angew Chem Int Ed*. 2005;44(14):2132-2135.
13. Adzic RR, Zhang J, Sasaki K, et al. Platinum monolayer fuel cell electrocatalysts. *Top Catal*. 2007;46(3):249-262.
14. Wang G, Cao D, Yin C, Gao Y, Yin J, Cheng L. Nickel foam supported-Co_3O_4 nanowire arrays for H_2O_2 electroreduction. *Chem Mater*. 2009;21(21):5112-5118.
15. Ramu R, Wanna WH, Janmanchi D, et al. Mechanistic study for the selective oxidation of benzene and toluene catalyzed by $Fe(ClO_4)_2$ in an H_2O_2-H_2O-CH_3CN system. *Mol Catal*. 2017;441:114-121.
16. Mourzina YG, Offenhäusser A. Electrochemical properties and biomimetic activity of water-soluble meso-substituted Mn(III) porphyrin complexes in the electrocatalytic reduction of hydrogen peroxide. *J Electroanal Chem*. 2020;866:114159.
17. Saravanan N, Mayuri P, Huang S-T, Kumar AS. Electrochemical immobilization of $[Mn(bpy)2(H_2O)_2]^{2+}$ complex on MWCNT modified electrode and its electrocatalytic H_2O_2 oxidation and reduction reactions: a Mn-pseudocatalase enzyme bio-mimicking electron-transfer functional model. *J Electroanal Chem*. 2018;812:10-21.
18. Zhou S, Pan W, Chen C, Lin L, Guo W. One pot synthesis of Fe_2O_3-reduced graphene nanocomposite as cathode material for Lithium Ion Batteries. *Int J Electrochem Sci*. 2021;16:210461.
19. Wu Z-P, Lu XF, Zang S-Q, Lou XW. Non-noble-metal-based electrocatalysts toward the oxygen evolution reaction. *Adv Funct Mater*. 2020;30(15):1910274.
20. Atwa M, Li X, Wang Z, et al. Scalable nanoporous carbon films allow line-of-sight 3D atomic layer deposition of Pt: towards a

new generation catalyst layer for PEM fuel cells. *Mater Horiz*. 2021;8(9):2451-2462.
21. Yang C, Wang H, Lu S, et al. Titanium nitride as an electrocatalyst for V(II)/V(III) redox couples in all-vanadium redox flow batteries. *Electrochim Acta*. 2015;182:834-840.
22. Mo H, Wang D, Chen Q, et al. Laser-assisted ultrafast fabrication of crystalline ta-doped TiO_2 for high-humidity-processed perovskite solar cells. *ACS Appl Mater Interfaces*. 2022;14(13):15141-15153.
23. Nayak SP, Ramamurthy SS, Kiran Kumar JK. Green synthesis of silver nanoparticles decorated reduced graphene oxide nanocomposite as an electrocatalytic platform for the simultaneous detection of dopamine and uric acid. *Mater Chem Phys*. 2020;252:123302.
24. Mialon G, Gohin M, Gacoin T, Boilot J-P. High temperature strategy for oxide nanoparticle synthesis. *ACS Nano*. 2008;2(12):2505-2512.
25. Somorjai GA, Park JY. Molecular surface chemistry by metal single crystals and nanoparticles from vacuum to high pressure. *Chem Soc Rev*. 2008;37(10):2155-2162.
26. Xu Z, Shen C, Hou Y, Gao H, Sun S. Oleylamine as both reducing agent and stabilizer in a facile synthesis of magnetite nanoparticles. *Chem Mater*. 2009;21(9):1778-1780.
27. Shaik F, Milan R, Amirav L. Gold@carbon nitride yolk and core–shell nanohybrids. *ACS Appl Mater Interfaces*. 2022;14(18):21340-21347.
28. Tolaymat TM, El Badawy AM, Genaidy A, Scheckel KG, Luxton TP, Suidan M. An evidence-based environmental perspective of manufactured silver nanoparticle in syntheses and applications: a systematic review and critical appraisal of peer-reviewed scientific papers. *Sci Total Environ*. 2010;408(5):999-1006.
29. Mo X, Chan KC, Tse ECM. A scalable laser-assisted method to produce active and robust graphene-supported nanoparticle electrocatalysts. *Chem Mater*. 2019;31(19):8230-8238.
30. Forsythe RC, Cox CP, Wilsey MK, Müller AM. Pulsed laser in liquids made nanomaterials for catalysis. *Chem Rev*. 2021;121(13):7568-7637.
31. Horwood CA, Owusu-Ansah E, Shi YJ, Birss VI. Pulsed laser induced dewetting of Au thin films on Ta_2O_5 substrates. *Chem Phys*. 2021;541:110926.
32. Ren M, Zheng H, Lei J, et al. CO_2 to formic acid using Cu–Sn on laser-induced graphene. *ACS Appl Mater Interfaces*. 2020;12(37):41223-41229.
33. Wang W, Tse ECM. Proton removal kinetics that govern the hydrogen peroxide oxidation activity of heterogeneous bioinorganic platforms. *Inorganic Chem*. 2021;60(10):6900-6910.
34. Simon P, March K, Stéphan O, et al. X-ray absorption investigation of titanium oxynitride nanoparticles obtained from laser pyrolysis. *Chem Phys*. 2013;418:47-56.
35. Güntner AT, Pineau NJ, Pratsinis SE. Flame-made chemoresistive gas sensors and devices. *Prog Energy Combust Sci*. 2022;90:100992.
36. Wang K, Endo-Kimura M, Belchi R, et al. Carbon/graphene-modified titania with enhanced photocatalytic activity under UV and Vis irradiation. *Materials*. 2019;12(24):4158.
37. Mo X, Gao X, Gillado AV, et al. Direct 3D printing of binder-free bimetallic nanomaterials as integrated electrodes for glycerol oxidation with high selectivity for valuable C_3 products. *ACS Nano*. 2022;16(8):12202-12213.
38. Wei Z, Wang W, Li W, et al. Steering electron–hole migration pathways using oxygen vacancies in tungsten oxides to enhance their photocatalytic oxygen evolution performance. *Angew Chem Int Ed*. 2021;60(15):8236-8242.
39. Zeng T, Wu H-L, Li Y, Tse ECM, Barile CJ. Physical and electrochemical characterization of a Cu-based oxygen reduction electrocatalyst inside and outside a lipid membrane with controlled proton transfer kinetics. *Electrochim Acta*. 2019;320:134611.
40. Tse ECM, Barile CJ, Kirchschlager NA, et al. Proton transfer dynamics control the mechanism of O_2 reduction by a non-precious metal electrocatalyst. *Nat Mater*. 2016;15(7):754-759.
41. Tse ECM, Hoang TTH, Varnell JA, Gewirth AA. Observation of an inverse kinetic isotope effect in oxygen evolution electrochemistry. *ACS Catal*. 2016;6(9):5706-5714.
42. Tse ECM, Varnell JA, Hoang TTH, Gewirth AA. Elucidating proton involvement in the rate-determining step for Pt/Pd-based and non-precious-metal oxygen reduction reaction catalysts using the kinetic isotope effect. *J Phys Chem Lett*. 2016;7(18):3542-3547.
43. Husain S, Akansel S, Kumar A, Svedlindh P, Chaudhary S. Growth of Co_2FeAl Heusler alloy thin films on Si(100) having very small Gilbert damping by ion beam sputtering. *Sci Rep*. 2016;6(1):28692.

SUPPORTING INFORMATION

Additional supporting information can be found online in the Supporting Information section at the end of this article.

How to cite this article: Mo X, Bouchet Fabre B, Herlin-Boime N, Tse ECM. Rapid laser synthesis of surfactantless tantalum-based nanomaterials as bifunctional catalysts for direct peroxide–peroxide fuel cells. *SmartMat*. 2023;e1181. doi:10.1002/smm2.1181